Aggregation behaviour of magnetic nanoparticle suspensions investigated by magnetorelaxometry

D Eberbeck, F Wiekhorst, U Steinhoff and L Trahms

Department 8.2 Biosignals, Physikalisch-Technische Bundesanstalt, Abbestraße 2-12, 10587 Berlin, Germany

E-mail: dietmar.eberbeck@ptb.de

Abstract
The aggregation behaviour of magnetic nanoparticles (MNP) is a decisive factor for their application in medicine and biotechnology. We extended the moment superposition model developed earlier for describing the Néel relaxation of an ensemble of immobilized particles with a given size distribution by including the Brownian relaxation mechanism. The resulting cluster moment superposition model is used to characterize the aggregation of magnetic nanoparticles in various suspensions in terms of mean cluster size, aggregate fraction, and size dispersion. We found that in stable ferrofluids 50%–80% of larger magnetic nanoparticles are organized in dimers and trimers. The scaling of the relaxation curves with respect to MNP concentration is found to be a sensitive indicator of the tendency of a MNP suspension to form large aggregates, which may limit the biocompatibility of the preparation. Scaling violation was observed in aged water based ferrofluids, and may originate from damaged MNP shells. In biological media such as foetal calf serum, bovine serum albumin, and human serum we observed an aggregation behaviour which reaches a maximum at a specific MNP concentration. We relate this to agglutination of the particles by macromolecular bridges between the nanoparticle shells. Analysis of the scaling behaviour helps to identify the bridging component of the suspension medium that causes agglutination.

1. Introduction

The relaxing magnetization of an ensemble of magnetic nanoparticles (MNP) suspended in a fluid medium after the application of an external magnetic field provides information on the motional state of the particles. If magnetic nanoparticles are used to label particular analytes, magnetorelaxometry may elucidate chemical or biochemical reactions. The distinction of Néel and Brownian relaxation mechanisms was shown to enable the binding specific detection of antibodies in a magnetic relaxation immunoassay (MARIA) [1–10].

Magnetorelaxometry (MRX) is also a useful tool for characterizing the magnetic cores of nanoparticles. In the absence of a suspension medium, magnetic nanoparticles are immobilized and only Néel relaxation remains an effective mechanism of relaxation, which strongly depends on the core size of the particles. In this case, the core size distribution of the particles can be quantified by applying the previously developed moment superposition model (MSM) to the relaxation signal [11].

Here, we modify this approach to model the behaviour of magnetic nanoparticles in suspension, where Brownian and Néel processes simultaneously contribute to the relaxation of the magnetization. To this end, we extend the MSM by including also the Brownian mechanism. In our experimental set-up, we have sensitivity to the Brownian relaxation of small and medium particle clusters and the Néel relaxation of particles in large clusters.

We show that this opens the option to study the aggregation behaviour of magnetic particles. Aggregation is a most important issue for virtually all biomedical applications of MNP suspensions, because aggregation may not only compromise the intended diagnostic or therapeutic effect, for *in vivo* applications it may even cause dramatic side effects such as thrombosis.

In this paper we will outline the methodical background of studying MNP aggregation by MRX. This includes the physical background of MRX, adequate instrumental equipment, dedicated signal acquisition and processing tools, as well as the modelling background for the data analysis in terms of the cluster superposition model. In addition, we give an overview on the interaction forces between magnetic nanoparticles, which are responsible for the observed aggregation phenomena. A number of studies on the aggregation of various magnetic nanoparticle preparations suspended in a variety of media, such as water, phosphate buffered saline, foetal calf serum, bovine serum albumin, and human serum, illustrate the applicability of the method.

2. Physical background

2.1. Magnetic relaxation

The response of ferromagnetic material to sudden changes of an external applied field often shows a time lag. This phenomenon has long been studied and is commonly referred to via the notions 'magnetic viscosity' or 'after effect' [12, 13]. If a similar experimental procedure is applied to a system of magnetic nanoparticles, this gives rise to relaxation phenomena that are different from what happens in bulk material. The particular physics of magnetic nanoparticles make them suited for labelling biological molecules, in order to analyse their chemical binding behaviour by magnetorelaxometry, as we will call the procedure in this paper.

Magnetic nanoparticles consist of a material that is ferromagnetic or ferrimagnetic as bulk. Due to their small core diameters of 4–200 nm, they form a single domain of uniform magnetization having a total magnetic moment μ given by

$$\mu = M_S V_p, \tag{1}$$

where M_S denotes the saturation magnetization and V_p the volume of the core of the particle. Due to an effective magnetic anisotropy K, which generally arises from a combination of shape and magnetocrystalline anisotropy, the magnetic moments have preferred orientations, so-called easy axes representing local energy minima.

If an external magnetic field of sufficient strength and duration is applied to a sample containing magnetic nanoparticles, the magnetic moments of the particles will align and sum up to a net magnetization $\mathbf{M}$ $(t = 0)$ of the sample along the field direction. After the external

field is switched off, the decay of the magnetization gives rise to a time dependent magnetic flux density $\mathbf{B}(t)$ measured at the sensor position. For an ensemble of identical particles, an exponential decay is expected:

$$B(t) = B_0 \exp\left(-t/\tau\right), \qquad (2)$$

where τ is the relaxation time and the starting value $B_0 = B(t = 0)$ is the magnetic flux density generated by the initial magnetic dipolar moment of the sample.

Two different mechanisms responsible for the relaxation of the magnetization of ferrofluids should be distinguished. One is the Brownian relaxation, where the magnetic nanoparticles suspended in the carrier fluid change their orientation by random Brownian rotation due to thermal activation. The time decay of the magnetic moment associated with this rotational diffusion is described by the Brownian relaxation time τ_B [14]

$$\tau_B = \frac{3\eta V_{\text{hydr}}}{k_B T}, \qquad (3)$$

where V_{hydr} is the hydrodynamic volume of the particle, including the core and the organic coating layer of the magnetic nanoparticle, η the viscosity of the carrier fluid, k_B the Boltzmann constant and T the temperature.

The magnetic moment may also change its orientation within the particle overcoming the energy barrier constituted by the anisotropy energy $E_A = K V_p$, which is proportional to the particle volume with the anisotropy constant K. The corresponding time decay of the magnetization is expressed by the Néel relaxation time τ_N [15]

$$\tau_N = \tau_0 \exp\left(\frac{K V_p}{k_B T}\right), \qquad (4)$$

with τ_0 having values in the range from 10^{-9} to 10^{-11} s. If both relaxation processes are present, the mechanism with the shortest relaxation time will be dominant resulting in an effective relaxation time τ_{eff} [16]

$$\tau_{\text{eff}} = \frac{\tau_N \tau_B}{\tau_N + \tau_B}. \qquad (5)$$

Therefore, the relaxation of the moments of suspended MNP is always faster than that of immobilized particles. This is the key property for distinguishing between relaxation curves of free and immobilized MNP.

2.2. Relaxation curves

2.2.1. Phenomenological description. It is obvious from equation (4) that the magnetic relaxation strongly depends on the particle size. Two parameters provide a rough characterization of the relaxation curve. One is the relaxation amplitude ΔB, which is the magnetic field difference between two arbitrarily selected time points that stay constant during evaluation of all measurements, in most cases the first and last data point are taken. ΔB characterizes the magnetic moment of the nanoparticle sample. The other parameter is the effective relaxation time $t_{1/e}$ being the time interval in which the initially measured magnetic field value has dropped by the factor e.

In a real nanoparticle system, there is always a distribution of particle sizes. Under the assumption that the sizes of MNP (which contribute to the signal) are equally distributed, the relaxation curves can be described by [17, 18]

$$B(t) = B_0 \ln\left(1 + t_c/t\right) + B_{\text{offs}}, \qquad (6)$$

where t_c is a characteristic time depending on magnetization field and time, and particle anisotropy. B_{offs} accounts for the contribution of the remanent magnetization.

Alternatively, $B(t)$ can be described phenomenologically by fitting a stretched exponential,

$$B(t) = B_0 \exp\left[-(t/\tau)^\gamma\right] + B_{\text{offs}}, \tag{7}$$

where τ is interpreted as a characteristic relaxation time and γ as a measure of the width of the relaxation time distribution.

2.2.2. Moment superposition model. Often, the logarithmic normal distribution $P(V)$ is taken to describe the core particle size distribution

$$P(V) = \frac{1}{\sqrt{2\pi}\,\sigma\,V} \exp\left(-\frac{\ln^2\left(V/V_{\text{p}}\right)}{2\sigma^2}\right). \tag{8}$$

V_{p} is the median particle volume and σ the standard deviation of the distribution. As a consequence, this also entails a distribution of energy barriers and relaxation times.

A straightforward model describing the Néel relaxation of the magnetization of a system of magnetic nanoparticles is the moment superposition model, hereafter termed MSM [11, 17],

$$B(t) = g_{\text{sys}} M_{\text{S}} \int_V \mathrm{d}V\, V\, P(V)\, L(V, H, T) \left[1 - \exp\left(-\frac{t_{\text{mag}}}{\tau_{\text{eff}}(K, V, H, T)}\right)\right]$$
$$\times \exp\left(-\frac{t}{\tau_{\text{eff}}(K, V, T)}\right) + B_{\text{offs}}. \tag{9}$$

In this model, the magnetic parameters like saturation magnetization M_{S}, effective anisotropy K_{eff} and median V_{p} and standard deviation σ of the particle size distribution are taken into account, explicitly, as well as the experimental variables amplitude H and duration t_{mag} of the applied magnetic field. The expression in the first bracket of the right-hand side of equation (9) describes the relaxation of the magnetic moments during the magnetizing period of length t_{mag} before the relaxation measurement.

The magnetization reached by the magnetizing field at a temperature T is adjusted by the Langevin function

$$L(V, H, T) = \coth\left(\frac{\mu V \mu_0 H}{k_{\text{B}} T}\right) - \left(\frac{k_{\text{B}} T}{\mu V \mu_0 H}\right). \tag{10}$$

We assume a random orientation of anisotropy axes in our sample and explicitly take into account the field dependence of the Néel relaxation time extending equation (4) by [11]

$$\tau_{\text{N}}(K, V, H, T) = \tau_0 \exp\left(\frac{KV}{k_{\text{B}} T}\left(1 - \frac{0.82\mu_0 H M_{\text{S}}}{K}\right)\right), \tag{11}$$

which enters the effective relaxation time τ_{eff} defined in equation (5). The prefactor g_{sys} in equation (9) contains the geometrical factor of the experimental set-up as well as the concentration of the magnetic material in the sample.

Figure 1 shows theoretical relaxation curves at room temperature modelled for a typical nanoparticle suspension using the MSM model. For the calculation three different hydrodynamic diameters were assumed exemplifying the transition from a prevailing Brownian to a pure Néel relaxation. The other parameters were $M_{\text{S}} = 400$ kA m^{-1}, $K_{\text{eff}} = 7$ kJ m^{-3}, $d_{\text{p}} = 6.1$ nm, $\sigma = 1.35$ (volume), $\eta = 1$ mPa s, $H = 1600$ A m^{-1}, $t_{\text{mag}} = 1$ s. As can be seen from the figure, the relaxation becomes slower with increasing hydrodynamic diameter. So, first for fluid samples with particles having a hydrodynamic diameter larger than about 70 nm the relaxation curves fall into the measurement time window ($t_{\text{start}} = 500\,\mu\text{s} \ldots t_{\text{end}} = 0.5$ s). Its upper limit corresponds, according to equation (3), to a hydrodynamic diameter of 1 μm. This means, our MRX set-up predominantly measures entities (e.g. single particles, aggregates)
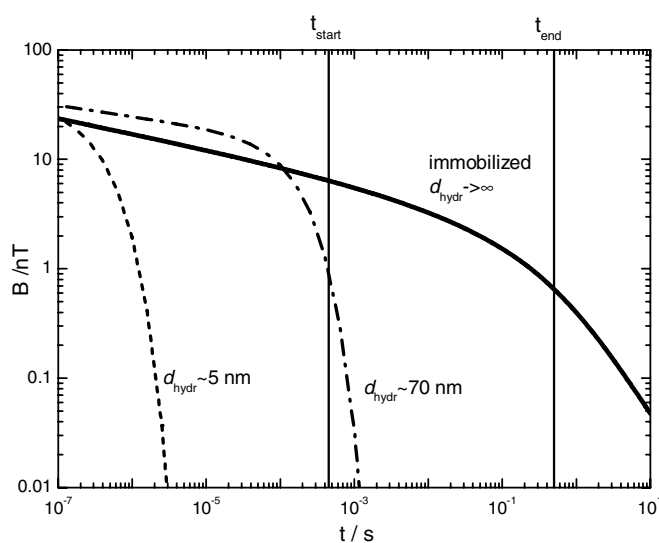
Figure 1. Theoretical room temperature relaxation curves for magnetic nanoparticles with three different hydrodynamic diameters showing the slowing down of the relaxation with increasing hydrodynamic diameter.

with hydrodynamic diameters between 70 nm and 1 μm. Above this upper limit, we mainly measure magnetic moments relaxing via the Néel process, which is the exclusive relaxation path for immobilized MNP.

According to the Néel equation (4), the relaxation amplitude of immobilized nanoparticles crucially depends on the core size. Reversing equation (4), the start and end times of our measurement correspond to particle diameters of 26 nm and 29 nm, respectively, assuming $K_{\mathrm{eff}} = 7$ kJ m^{-3}. That is, a relatively small fraction of larger particles causes the major part of the relaxation signal. It follows that our measurement data contain information primarily about the behaviour of these large particles.

Magnetorelaxometry allows the distinction between relaxation curves of free and immobilized MNP, which in turn can be exploited to assess the binding state of magnetic nanoparticles. With that, we already quantified the amount of MNP bound to latex beads and yeast cells [19, 20].

The different shapes of relaxation signals of bound or unbound nanoparticles allow us to separate the two contributions from a single measurement without any further washing step. Since an MRX measurement can be performed at intervals of a few seconds, it may be used as a tool to monitor the binding kinetics of a reaction that proceeds within a corresponding time interval. For a series of consecutive measurements, the amount β of bound magnetic nanoparticles is determined by fitting the following model to the data

$$B(t) = \beta B_{\mathrm{b}}(t) + (1 - \beta) B_{\mathrm{ub}}(t) + B_{\mathrm{offs}}. \tag{12}$$

The reference signals for bound and unbound nanoparticles (B_{b}, B_{ub}) are generated from initial measurements on liquid and freeze-dried samples.

2.2.3. Cluster moment superposition model. To account for the formation of clusters of magnetic nanoparticles due to aggregation of the nanoparticles, we extended the moment

superposition model (MSM) equation (9) to the cluster moment superposition model (cluster-MSM). The cluster-MSM allows the description of the magnetic relaxation of MNP belonging to clusters assuming a log-normal size distribution according to equation (8), now with V_c and σ_c as the median and the standard deviation of the cluster volumes. This leads to an additional volume integration in equation (9) to get the time decay of the magnetic flux density by

$$B_c(t) = g_{sys}\mu_0 M_S \int_{V_c} dV' P_c(V') \int_V dV\, P_p(V)\, V\, L(V, H, T)$$
$$\times \left(1 - \exp\left\{\frac{t_{mag}}{\tau_{eff}(K, V, V', H, T)}\right\}\right) \exp\left\{\frac{t}{\tau_{eff}(K, V, V', T)}\right\} + B_{offs}. \quad (13)$$

Now, the cluster volume V' determines the Brownian relaxation time τ_B in the expression for the effective relaxation time τ_{eff} equation (5). Considering that only a fraction ϕ_c of MNP belongs to clusters, the total flux density of a sample is calculated as

$$B(t) = \phi_c B_c(t) + (1 - \phi_c)B_p(t), \quad (14)$$

where the contribution of singlet particles $B_p(t)$ is calculated according the MSM equation (9). Fitting equation (14) to our data, the size distribution parameters of the clusters can be obtained. It is advantageous to estimate independently the parameters K_{eff}, V_p and σ_p of the particle size distribution by fitting equation (9) to the relaxation curves of freeze dried samples from the same stock suspension. By this the number of adjustable parameters of the cluster-MSM reduces to four: ϕ_c, V_c, σ_c and B_{offs}.

The fit may still be an ill-conditioned inverse problem, where stable solutions are difficult to achieve, in particular in the presence of a poor signal to noise ratio. In order to compare the relaxation curves over the whole measured concentration range we parametrize the curves for low MNP concentration by the parameter $t_{1/e}$ and calculate a mean cluster size according to

$$d_c^{mean} = d_{c,ref}^{mean}(t_{1/e}/t_{1/e,ref})^{1/3}, \quad (15)$$

where we have introduced a mean cluster size $d_c^{mean} = (6V_c \exp(\sigma_c^2/2)/\pi)^{-1/3}$ corresponding to the median cluster volume V_c of the cluster distribution, for convenience. $d_{c,ref}^{mean}$ is the mean cluster size of a reference sample with higher MNP concentration, provided this reference shows a relaxation curve which can be described by equation (14), i.e. without any obvious multimodal cluster size distribution, indicating instabilities or irregularities. The results obtained by equation (15) become more stable, since we discard additional information about aggregate fraction ϕ_c and cluster size distribution σ_c.

2.3. Interactions between magnetic nanoparticles

In a ferrofluid, e.g. an aqueous suspension of magnetic nanoparticles, the superparamagnetic core usually is surrounded by a shell of an organic material serving to prevent aggregation. For the use in biological systems, the shell should additionally ensure biocompatibility.

In order to understand the aggregation behaviour of various MNP in different suspension media it is instructive to elucidate the main interaction energies of magnetic dipolar, van der Waals, electrostatic and steric interaction which depend crucially on the structural parameters of the MNP. While the two former interactions generate attractive forces, the latter two interactions have repulsive character. If the resulting total interaction energy has a minimum being much deeper than $k_B T$, then instability, i.e. aggregation of these particles, is likely to occur.

In figure 3, these individual interaction energy contributions have been calculated according to the formulae given in the appendix as a function of the distance separating the core surfaces $s + 2\delta$ of MNP having a core diameter d_p of 15 nm for two different shell thicknesses $\delta = 4$ nm and 20 nm, respectively (see figure 2). In the case of thin shells the dipole–dipole
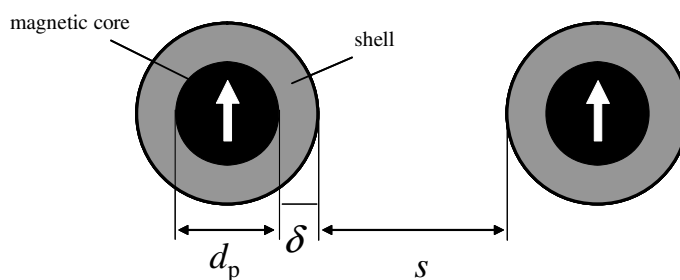
Figure 2. Sketch of two core–shell MNP with the geometric parameters which determine the interaction energy. The white arrows symbolize the magnetic moments of the single domain cores.
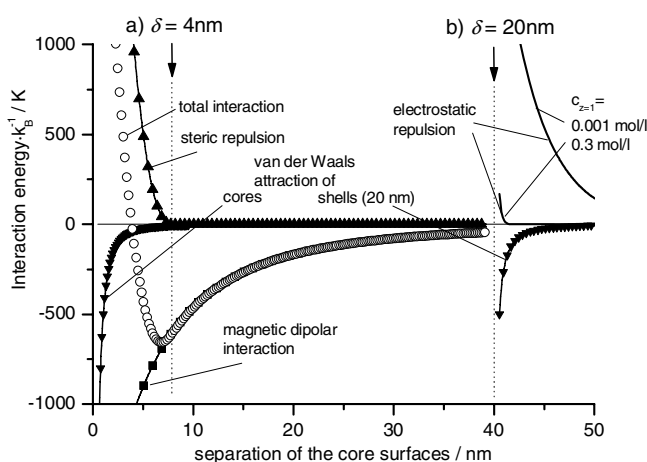

Figure 3. Calculated interaction energy contributions for particles with $d_p = 15$ nm core diameter and $M_S = 400$ kA m^{-1} and Young's modulus $E = 10^6$ Pa with (a) shell thickness $\delta = 4$ nm, van der Waals interaction (between the cores only) $A_c = 17 \times 10^{-20}$ J and $A_w = 4.4 \times 10^{-20}$ J, surface potential $\Psi = 0$. (b) $d_p = 15$ nm, shell thickness $\delta = 20$ nm, van der Waals interaction (between the shells only) $A_s = 7 \times 10^{-20}$ J, $A_w = 4.4 \times 10^{-20}$ J, $\Psi = 60$ mV and two concentrations of monovalent ions of $c_{z=1} = 0.001$ and 0.3 mol l^{-1} (typical for PBS). The dotted lines mark the core surface distance where the shells are in contact.

interaction is the dominating attracting energy (figure 3(a)). Together with the steep increasing steric repulsion potential the minimum of the total interaction energy is near the surface of the shell. For aligned and parallel magnetic moments the corresponding potential minimum is deeper than thermal energy at room temperature, thus enabling aggregation.

For thicker shells (figure 3(b)), the van der Waals interaction between the shells becomes the leading contribution provided the Hamaker constants of shell and suspension medium differ remarkably (table 1). Then, a repulsive interaction other than steric is necessary to prevent aggregation, for example, electrostatic interaction. But, if these particles are used in media with high salt concentration, e.g. PBS, the ions screen the electrostatic potential, possibly causing aggregation.

In the case of a solvated (water filled) surfactant layer, where the surfactant content of the shell is reduced to a volume fraction ϕ, the Hamaker constant of the shell is approximated by $A_{ss} \approx (\phi A_{ss}^{1/2} + (1 - \phi) A_{ww}^{1/2})^2$ [21]. The corresponding values in table 1 show that a solvation

Table 1. Composite Hamaker A_{ii} constants for components (i = c, s) of core–shell MNP in vacuum and water ($A_{ii(w)}$) [22]. (Note: $A_{ii,\text{solv}}$: Hamaker constants where the component i is enriched by water, i.e. solvatized. Here, $\phi = 0.25$ is the volume fraction of the non-aqueous part of a solvated shell.)

Material	A_{ii} (10^{-20} J)	$A_{ii(w)}$ (10^{-20} J)	$A_{ii,\text{solv}}$ (10^{-20} J)	$A_{ii(w),\text{solv}}$ (10^{-20} J)
			Solvatized, $\phi = 0.25$	
Water	4.4	0		
Alkane ($n = 18$)	8	0.53	5.2	0.033
Polystyrene	9	0.80		
BSA	8.4	0.65	5.3	0.041
Silica	7	0.30[a]		
Metal oxide (Al_2O_3)	17	4.1		

[a] Experimental value estimated for aqueous sample.

of the shell reduces the van der Waals interaction energy of the MNP by about one order of magnitude.

3. Materials and methods

3.1. Magnetorelaxometer set-up

In a typical magnetorelaxometry experiment, a sample of 150 μl volume (polystyrene microtitre vial) is placed in the 10 mm bore of the magnetizing coil. Magnetic fields of up to 2 kA m^{-1} are applied for 1 s to align the magnetic moments of the particles in the sample into the z-direction. Starting 500 μs after switching off the magnetizing field, the decay of the magnetic induction $B(t)$ in z-direction is detected by a low T_c superconducting quantum interference device (SQUID) at a distance of 10 mm above the sample. The SQUID sensor has a sensitivity of 0.463 nT/Φ_0 and is mounted at the bottom of the tail of a Dewar vessel filled with liquid helium. An additional second SQUID at a distance of 12 cm above the sample allows the gradiometric compensation of far field magnetic distortions.

The SQUID readout electronics has a bandwidth from dc to several megahertz and a dynamic range of ± 235 nT over a noise floor of 1.5 fT Hz$^{-1/2}$ of the SQUIDs. The total system noise amounts to 7 fT Hz$^{-1/2}$ at 1 kHz. Using twin coils, i.e. parallel coils with opposite polarity, for the magnetization procedure, the stray field at the SQUID location can be reduced by several orders of magnitude. Additionally, the relaxometer is operated in a magnetically shielded room suppressing environmental magnetic noise from outside.

Over the time period between 500 μs up to 0.5 s after switching off the field the relaxation signal is digitized with a sampling rate of 100 kHz and 16 bit word length. The short duration of one measurement makes repetitive measurements feasible. Thus, the signal to noise (SNR) ratio can be improved by signal averaging.

In addition to the measurement of the sample containing nanoparticles, usually a measurement of an empty vial is carried out under the same conditions to account for background signals from the coil and the vial.

3.2. Data preprocessing

A magnetic relaxation signal is characterized by fast amplitude changes at its beginning and a much slower decay at later time instants. To follow the rapidly changing first part of the relaxation signal, a high bandwidth of sensor, electronics and digitizing unit is necessary. This requirements are no longer necessary in later parts of the signal, where in turn a better amplitude

resolution would be helpful to improve the signal to noise ratio. This dilemma can be solved by introducing a preprocessing step after digital data acquisition which resamples the data in logarithmically scaled time intervals using appropriate adaptive antialiasing filters.

To this end, the following formula defines N sampling points t_i separated by logarithmically increasing steps within an arbitrary interval $(t_{start} \ldots t_{end})$

$$t_i = t_{start} \left(\frac{t_{end}}{t_{start}} \right)^{i/N}, \qquad \text{where } i = 1 \ldots N. \tag{16}$$

Since the signal is originally digitized with a constant sampling interval Δt_{ori} by the A/D converter of the recording hardware, the time points t_i are approximated by interpolation to the closest original sampling point t_{ori}.

In order to drop off data points between the sample points t_i, it is necessary to apply first an appropriate low pass filter to the data. The filter frequency depends on the interval Δt_i between two sampling points and has to be adapted continuously. This interval is calculated as

$$\Delta t_i = \Delta t_{ori} + t_{start} \left(\left(\frac{t_{end}}{t_{start}} \right)^{\frac{i+1}{N}} - \left(\frac{t_{end}}{t_{start}} \right)^{\frac{i}{N}} \right). \tag{17}$$

If the calculated distance Δt_i is smaller than the original sample interval, the original sample points should be used and no filtering is necessary. In all other cases, the original signal is resampled, using the sample interval calculated by equation (17).

Before resampling the data, an appropriate antialiasing low pass filter with variable border frequency given by $f_{g,i} = 1/2 \Delta t_i^*$ is applied to the interval of original sampling points (t_{i-1}^*, t_i^*) to avoid the violation of the Nyquist theorem. This procedure ensures an optimized trade-off between amplitude resolution and bandwidth for every time interval.

After logarithmic resampling follows a background correction by subtracting the signal from the empty vial measurement. Furthermore, we subtract the last measured data point from the signal. This removes the actual SQUID offset, which is meaningless, since SQUID sensors only detect relative changes in the magnetic field. In addition, this cancels from the signal any remanent contributions of those nanoparticles, which have not relaxed in the measurement time interval. A ten per cent offset of the relaxation amplitudes is added for graphical presentation, because usually, relaxation curves are displayed on a double logarithmic scale.

3.3. Magnetic nanoparticles and suspension media

All MNP investigated were core–shell composite particles with a magnetic core consisting of magnetite/maghemite or cobalt ferrite, surrounded by a polymer surfactant layer or a silica shell. An exception are MPScaps, small clusters of primary magnetite cores encapsulated in a polystyrene bead obtained by a miniemulsion technique [25]. The carrier fluid of all MNP were aqueous based. Details of the MNP investigated in this study can be found in table 2.

As suspension media we used aqua destillata (aqua dest), phosphate buffered saline (PBS) containing 0.14 mol l^{-1} NaCl, bovine serum albumin (BSA) with an albumin concentration of 10% by weight, i.e. $1.5 \times 10^{-3} \text{ mol l}^{-1}$, foetal calf serum (FCS) with an albumin concentration of about 2% by weight or $0.3 \times 10^{-3} \text{ mol l}^{-1}$ and a concentration of γ-immunoglobulin of 0.02% (Sigma Aldrich, Datasheet F7524). Because most of the γ-immunoglobulins are antibodies, their content is roughly estimated to be $1.3 \times 10^{-6} \text{ mol l}^{-1}$. In FCS exclusively IgG antibodies are present. Human serum was purchased from Sigma Aldrich (order No: S7023). For a similar sample (Sigma Aldrich, Datasheet H4522) an albumin concentration of about 3.5% or $0.6 \times 10^{-3} \text{ mol l}^{-1}$ and an antibody concentration of about $3.3 \times 10^{-5} \text{ mol l}^{-1}$ is reported.

Table 2. Survey of the investigated MNP samples.

MNP sample	Producer	Core	Iron (+cobalt) concentration c(Fe, Co) (mol l^{-1})	Particle shell	Zeta potential[a] ζ (mV)
			Charged shell		
CoFeTESPMA	Fischer [33]	CoFe$_2$O$_4$	0.015	Silica, TESPMA[b]	−60
DDM128N	Meito Sangyo, Japan	Fe$_3$O$_4$/γ-Fe$_2$O$_3$	1.0	Carboxydextran	−40
FluidMag-AS	Chemicell GmbH	Fe$_3$O$_4$	0.27	Acrylic acid	−40
MagBSA	Koneracká [29]	Fe$_3$O$_4$	0.144	BSA[c]	−41
MPScap	Ramírez [25]	Fe$_3$O$_4$		Polystyrene/SDS[d]	[e]
μ MACS*SA	Miltenyi Biotec	Fe$_3$O$_4$/γ-Fe$_2$O$_3$			
Resovist	Schering AG	Fe$_3$O$_4$/γ-Fe$_2$O$_3$	0.5	Carboxydextran	≈−30
			Non-charged shell		
FluidMag-D5	Chemicell GmbH	Fe$_3$O$_4$	0.73	Starch	≈0
FluidMag-D3030	Chemicell GmbH	Fe$_3$O$_4$	0.13	Starch	≈0

[a] In water.
[b] TESPMA: triethylsilylpropylmaleamic acid.
[c] BSA: bovine serum albumin.
[d] SDS: sodium dodecylsulfonate.
[e] 1.53 carboxyl groups per nm^2 particle surface.

For checking the binding effect of the antibodies we used tempered serum (60 °C for 40 min), because by tempering the immunological complement system [26] and the antibodies [27, 28] lose their binding capacity.

The preparation of the samples was performed by successive dilution. For example, 450 μl of the suspension medium of interest were filled in a 0.5 ml polyethylene tube. Then, 50 μl of the MNP stock suspension were added by pipetting resulting in a 1:10 diluted sample. For a 1:100 dilution, the procedure was repeated using the 1:10 diluted sample instead of the stock suspension.

4. Experimental results and discussion

4.1. Estimation of aggregate size distributions

On the basis of the cluster moment superposition model (cluster-MSM) outlined in section 2.2.3, we can interpret magnetization decays obtained by magnetorelaxometry on suspensions of various magnetic nanoparticles in various aqueous solutions, such as water, PBS, BSA, and FCS. In figure 4 relaxation data for fluid DDM128 particles in different suspending media are presented together with a best fit according to equation (14).

The amplitude Φ_c predominantly represents the fraction of particles that have effective relaxation times τ_{eff} given by equation (5) within the measurement time window, so that they can contribute to the observed relaxation.

In particular, these are aggregates containing MNP with a diameter $d_c \geqslant 20$ nm. For DDM128 in water, the fraction of detectable MNP is $\Phi_c = 0.69$, indicating that a little less than one third of the particles is not aggregated in stable clusters that are detectable by MRX. It is different in more viscous media like FCS, where with $\Phi_c = 1$, all particles with
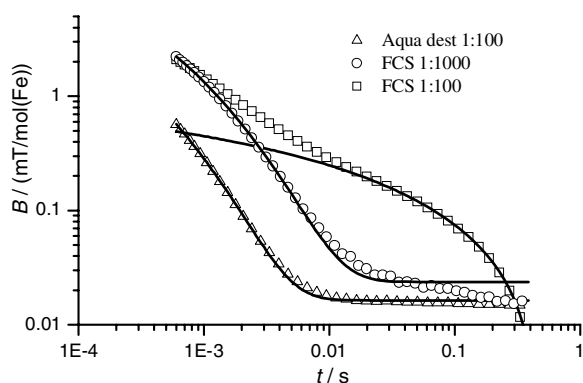
Figure 4. Relaxation curves (measured May 2005) of DDM128N samples suspended in aqua dest and FCS, respectively, together with cluster-MSM fit curves according to equation (14). The following fit parameter were obtained, aqua dest (1:100): $\Phi_c = 0.69(3)$, $d_c = 51(2)$ nm, $\sigma_c = 0.422(5)$; FCS (1:100): $\Phi_c = 0.068(3)$, $d_c = 141(80)$ nm, $\sigma_c = 1.0(1)$; FCS (1:1000): $\Phi_c = 1.00(3)$, $d_c = 58(3)$ nm, $\sigma_c = 0.411(5)$. For the fit of the sample 1:100 diluted in FCS, only data points for $t > 0.02$ s were used and the fit curve extrapolated to shorter times.

$d_c \geqslant 26$ nm contribute to the observed relaxation. This can be caused by the high magnetic dipolar interaction energy of these large particles with $\delta = 4$ nm (figure 3).

The relaxation curve of DDM128N suspended in FCS (1:100) differs qualitatively from the other preparations shown in figure 4. The shape can be analysed as a superposition of two curves, originating from the faster relaxation of small aggregates and free particles, and the slower relaxation of larger aggregates. For the latter, we found that this relaxation can be described by aggregates which have a very broad size distribution ($\sigma = 1$) but which involve only about 7% of the MNP (figure 4). This will be discussed in section 4.3.

In the case where DDM128N is diluted in aqua dest by a ratio of 1:100, we obtain a mean diameter of the particle clusters d_c^{mean} that is consistent with the data obtained by independent magneto-optical measurement ('MORFF') [30]. Similar agreement was found between our cluster size analysis of MRX measurements on fluid aqueous preparations of Resovist and cobalt ferrite particles CoFeTESPMA and data obtained by photo correlation spectroscopy (table 3). Diameters of $d_v = 50\ldots 80$ nm correspond to dimers or trimers of MNP with a shell thickness of about $\delta = 4$ nm. This is in agreement with molecular dynamics simulations by Wang and Holm [31], who found that the mean size of clusters of MNP with similar magnetic properties does not exceed 2.5 particle diameters.

4.2. Scaling of relaxation curves

A particular combination of MNP and suspending medium gives rise to a particular relaxation curve that characterizes its cluster size distribution. Usually, the amplitude of this curve is proportional to the MNP concentration while its shape remains unchanged, indicating that the size distribution of the clusters remains invariant. An example of this scaling behaviour of the relaxation curves, which was observed in many freshly prepared ferrofluids, is given in figure 5(a) for a commercially available magnetic resonance imaging contrast agent.

There are cases, however, where preparations of MNP suspensions exhibit a different behaviour upon a change of the MNP concentration. An example is given in figure 5(b), which shows relaxation curves of different concentrations for the same contrast agent 1.5 years after its expiration date. Still no precipitation was visible by eye, but apparently, the fraction of large
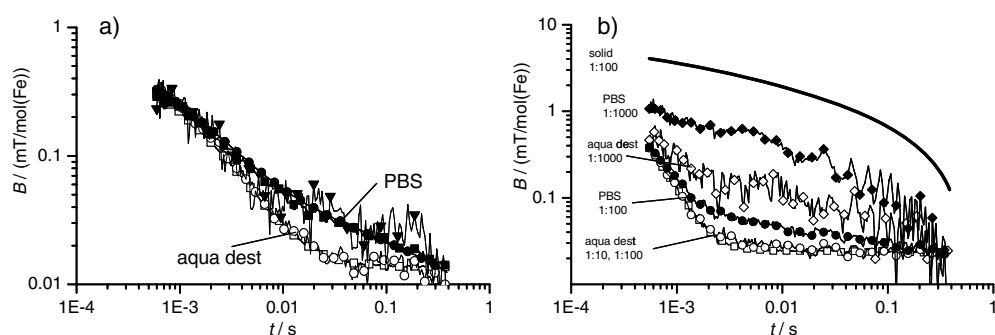
Figure 5. Scaling behaviour (relaxation curves normalized to iron concentration) of a commercial MRI contrast agent suspended in aqua dest (open symbols) and in PBS (filled symbols), respectively (a) in a fresh sample, dilution steps $1:10^2$, $1:10^3$. (b) Non-scaling in aged samples. For comparison the relaxation curve of a freeze dried sample 1:100 (solid line) has been added.

Table 3. Size distribution parameters of the cores and of the MNP clusters of investigated MNP suspended in aqua dest.

| MNP sample | Particle core | | | Cluster | | PCS | MORFF |
	$c(MNP)$ $(10^{-6}$ mol l$^{-1})$	d_p^{mean} (nm)	Φ_c	d_c^{mean} (nm)	σ_c	d_c^{mean} (nm)	d_c^{mean} (nm)
Charged shell							
CoFeTESPMA	0.87	9.3(2.0)	0.035(1)	59(9)	0.60(1)	65.5	
DDM128N	38	9.1(6)	0.69(4)	51(2)	0.42(1)		57(4)
FluidMag-AS	9.23	11(2)	0.75(2)	80(5)	0.34(4)		
MagBSA	70	4.6(2)	1.0(1)	77(2)	0.48(2)		
MPScap[a]	0.0053	—	—	—	—	72	
Resovist	38	8.5(1.0)	0.70(3)	54(2)	0.41(1)	60.7	
Non-charged shell							
FluidMag-D5	140	6.2(1.5)	0.90(3)	53(3)	0.46(1)		
FluidMag-D3030	18	7.9(1.0)	0.50(5)	83(6)	0.42(3)		

aggregates increases with dilution, i.e. with decreasing MNP concentration. In some cases, we observed relaxation curves that approached the relaxation of the freeze dried sample, indicating the presence of clusters that are in the μm range for which the Brownian relaxation time is too slow to be observed within the measurement time. In this case, Néel relaxation remains the only efficient mechanism as in freeze dried samples.

A plausible mechanism for increasing aggregation at lower concentrations could be the higher degree of partial dissolution of the surfactant layer molecules from the nanoparticle core due to a lower osmotic pressure of these molecules in the suspension. This should mainly happen in aged samples where the stability of the particle shell was affected by various processes. In fact, according to our observations, ageing appears to be an important cause for unstable MNP suspensions, in which the cluster size grows with the dilution. In many cases we observed visible precipitation of MNP in the samples hours up to days after the dilution procedure. Deviations from scaling of MRX signals appear to be an early indicator of this behaviour. This may make MRX particularly useful for the quality control of MNP suspensions like contrast agents which are routinely applied in medical physics.
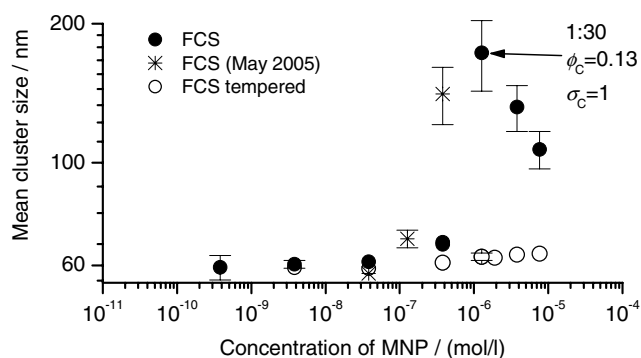
Figure 6. Mean cluster sizes of DDM128N in dependence of the MNP concentration with respect to FCS, obtained by fitting the cluster-MSM equation (14) to relaxation curves for $c(MNP) > 4 \times 10^{-8}$ mol l^{-1}. Where not indicated, measurements were performed in March 2006. At lower concentrations the size was estimated using $t_{1/e}$ and equation (15).
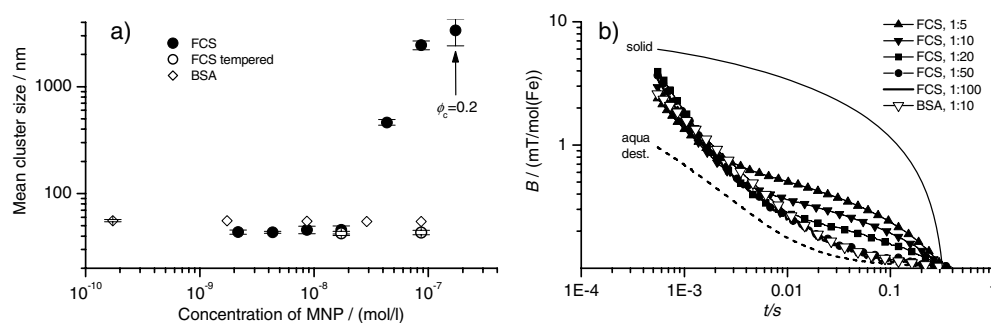

Figure 7. (a) Mean cluster sizes of CoFeTESPMA in dependence of the MNP concentration in FCS, BSA and aqua dest. As a reference obtained by fitting the cluster-MSM equation (14) to relaxation curves for $c(MNP) > 8 \times 10^{-9}$ mol l^{-1} in the case of FCS. Otherwise, the size was estimated according to equation (15). (b) Relaxation curves for CoFeTESPMA showing the rising of larger clusters in samples with a MNP to FCS ratio of 1:20, 1:10 and 1:5. The relaxation curves for more highly diluted suspensions in FCS are similar to that of BSA. For comparison purposes curves of aqueous and freeze dried suspensions are added.

Often, MNP are not only sterically but also electrically stabilized. Addition of ions screens this potential and reveals the influence of the steric repulsion potential. For freshly prepared negatively charged MNP, we found that scaling is preserved when the medium water is replaced by PBS, indicating that in this case steric interaction is a sufficient stabilization factor. On the other hand, in aged magnetic nanoparticle samples significant deviations from a scaling behaviour are observed, which is even more pronounced in PBS than in water (figure 5(b)). Apparently, electrical interactions are no longer sufficient to stabilize the suspension when the polymeric surfactant layer is affected.

4.3. Aggregation behaviour of MNP in FCS, BSA and human serum

Additionally, we investigated the aggregation behaviour of various magnetic nanoparticles samples in different media, such as FCS, BSA or human serum. The scaling of the relaxation curves was studied in terms of the mean cluster sizes, aggregate fraction and size dispersion obtained by fitting the cluster-MSM (14) (figures 6–9). At low MNP concentrations with a small SNR we used equation (15) and determined $t_{1/e}$ instead.
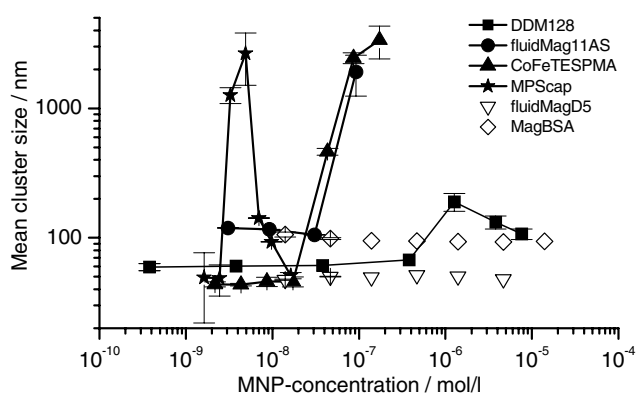
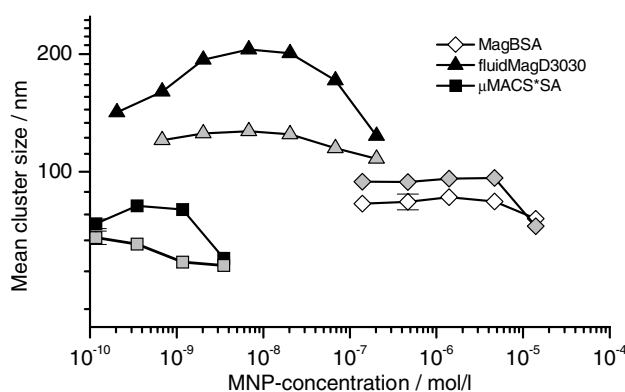**Figure 8.** Mean cluster sizes of various MNP after suspension in FCS.

Figure 9. Mean cluster sizes of indicated MNP suspensions prepared in human serum. The crossed symbols stands for tempered human serum as suspension medium.

Suspensions of fluidMag-D5 and MagBSA in FCS did not show any significant violation of scaling over the whole investigated concentration range. In contrast, suspensions of DDM128N, CoFeTESPMA, and MPScaps in FCS exhibited a clear maximum of the mean cluster size at different MNP concentrations as displayed in figure 8. This deviation from scaling is different from what was discussed in section 4.2 in that the cluster size increases with MNP dilution. We believe this behaviour to be caused by agglutination due to the bridging of nanoparticles by macromolecules of the suspension medium.

This binding between MNP and macromolecules could be realized for example by ion exchange binding, i.e. positively charged groups (e.g. amino groups) of the macromolecules (e.g. proteins) bind to negatively charged groups (e.g. carboxyl groups) of the MNP shell. Indeed, a common feature of the MNP showing agglutination in FCS is the presence of reactive carboxyl groups in the coating. And, uncharged MNP of fluidMag-D5 which do not have carboxyl groups do not show this agglutination phenomenon just as the negatively charged BSA-coated MNP (MagBSA).

In order to investigate whether this agglutination is caused by albumin, which is the most abundant protein in sera, we investigated the scaling behaviour of these MNP in BSA, which is more or less pure albumin. As shown in figure 7 for CoFeTESPMA, no larger aggregates emerge over the whole concentration range in BSA. This excludes albumin as the source of

agglutination and indicates that agglutination is caused by antibodies which are present in FCS, but not in BSA.

Agglutination is expected to be strongest for an optimal concentration ratio between MNP and macromolecules. For example, if both components are of the same size, their number density should be in the same range for maximum agglutination [22]. For DDM128N in FCS, aggregation is maximal at a MNP concentration of about 10^{-6} mol l^{-1} which is the same concentration as of the antibodies (IgG) in FCS. Furthermore, the size of an IgG molecule with a molecular mass of 150 000 g mol^{-1} of about 16 nm (approximately the largest distance in the molecule [32]) is close to the overall diameter d of a mean DDM128N particle, which is estimated to be $d = d_p^{mean} + 2\delta \approx 17$ nm with $d_p^{mean} \approx 9$ nm (table 3) and $\delta \approx 4$ nm. These data support the picture of agglutination of MNP mediated by antibodies.

In CoFeTESPMA, the maximum agglutination occurs at a MNP concentration of about 2×10^{-7} mol l^{-1} which is 50 times less than that of DDM128N (figure 8). This could be related to the much larger overall MNP diameter of about 65 nm caused by the large thickness of the silica coating. Accordingly, the interparticle surface of CoFeTESPMA is by a factor of $(65 \text{ nm}/10 \text{ nm})^2 \approx 40$ greater than that of DDM128. So, more antibodies can fill the space between MNP. The agglutination hypothesis is further supported by the observation that no agglutination occurs in tempered FCS, where thermal activation dissolves the bridges (see figure 6 for DDM128 and figure 7 for CoFeTESPMA).

In contrast, MPScaps, MNP in polystyrene beads, have a diameter of about 50 nm [25] which approximately is the same as for CoFeTESPMA, nevertheless, they show an agglutination maximum at a much lower concentration of 5×10^{-9} mol l^{-1}. The reason for this behaviour is not clear, but might point to a different binding process. So, this agglutination phenomenon might be based on a much lower antibody concentration as in the case of CoFeTESPMA.

Suspension of MNP in human serum also leads to an enhanced agglutination in a certain concentration range, except for MagBSA. In contrast to FCS, in human serum the aggregation maxima are broader extended over the concentration range (figure 9). Additionally, longer decay times of the corresponding relaxation curves indicate that the aggregate sizes in human serum suspensions have a wider distribution. The data could not be fitted by the cluster-MSM, possibly indicating that the size distribution deviates from log-normal type.

In human serum the concentration of antibodies is about 3×10^{-5} mol l^{-1} (see section 3.3), i.e. much higher than in FCS. It does not match with the investigated MNP concentration (figure 9). Nevertheless, the results indicate that also here agglutination takes place. Like for MPScaps in FCS, this agglutination may be caused by a different type of binding. Considering the low MNP concentration where agglutination of fluidMag-D3030 peaks in figure 9, it looks like only a very small fraction (1/100 000) of antibodies are responsible for this agglutination. This binding could be an immunologic reaction of a very small amount of specific antibodies with dextran molecules of the shell. As in FCS, tempering of human serum reduces agglutination. However, the effect is less pronounced as there still remains a small residual concentration depending aggregation.

MagBSA, magnetic nanoparticles coated with BSA, was the only sample investigated where scaling is preserved for almost all concentrations in human serum. Only at the highest concentration is there a small but significant decrease of the aggregate structure. Furthermore, this MNP does not show different behaviour in tempered human serum.

5. Conclusion

In this study we have pointed out how magnetorelaxometry can be used for the analysis and quantification of the aggregation behaviour of suspended MNP. To this end we developed the

cluster moment superposition model (cluster-MSM) on the basis of the moment superposition model intended for description of the Néel relaxation of immobilized particles.

By analysing the relaxation curves using the cluster-MSM we found that all investigated magnetite based MNP suspensions contain small clusters such as dimers or trimers. According to the cluster-MSM, 50%–80% of larger magnetic nanoparticles are organized in such clusters. This agrees well with the dipolar interaction energy of these larger particles in the aggregated state, which is calculated to be higher than the thermal energy.

The scaling of relaxation curves, i.e. the similarity of relaxation functions measured for different MNP concentrations, is a sensitive indicator of the stability of MNP suspensions with respect to aggregation. As a consequence of ageing, larger aggregates may form, possibly due to damage of the organic shell. The violation of the scaling behaviour of relaxation curves appears to be an early indicator for the instability of the suspension, i.e. for the tendency of the MNP to aggregate in larger clusters. MRX may be particularly useful for checking the stability of MNP suspended in different media, especially in non-transparent media where optical measurement methods may fail.

We found that MNP agglutinate in different biological media depending on the composition of the shell. The aggregation analysis developed in this study helps to identify the component of the medium causing the agglutination. Our measurements showed that MNP with a starch shell (fluidMag-D5) without functional groups and MNP with BSA shells (MagBSA) are most inert in different media. That means such particles are suitable for homogeneous binding assays because the relaxation properties of unbound markers remain unchanged.

Acknowledgments

Appendix

We consider two magnetic nanoparticles having a centre to centre distance of $r = s + d_{\mathrm{p}} + 2\delta$ with a core diameter d_{p} and a shell thickness δ (figure 2). The energy E_{m} corresponding to the magnetic dipole–dipole interaction between two identical magnetic moments $\boldsymbol{\mu}$ of the cores is written as

$$E_{\mathrm{m}}(r) = -\frac{\mu_0}{4\pi}\left(\frac{3\boldsymbol{\mu}\cdot(\boldsymbol{\mu}\cdot\mathbf{r})\,\mathbf{r}}{r^5} - \frac{\mu^2}{r^3}\right). \tag{A.1}$$

The van der Waals interaction energy E_{V} [21] of two core–shell particles suspended in water (w) is

$$E_{\mathrm{V}}(s,\delta) = -\tfrac{1}{12}\left(A_{\mathrm{cs}}H_{\mathrm{cs}} + A_{\mathrm{sw}}H_{\mathrm{sw}} + 2A_{\mathrm{cs}}^{1/2}A_{\mathrm{sw}}^{1/2}H_{\mathrm{cs(w)}}\right). \tag{A.2}$$

The indices denote the cs: core/shell (in vacuum), sw: shell/water (in vacuum), cs(w): core/shell in water as medium. The geometrical dimensions are absorbed in $H_{ij}(s,\delta)$

$$H_{ij}(s,\delta) = \frac{b_{ij}}{a_{ij}^2 + a_{ij}b_{ij} + a_{ij}} + \frac{b_{ij}}{a_{ij}^2 + a_{ij}b_{ij} + a_{ij} + b_{ij}} + 2\ln\left(\frac{a_{ij}^2 + a_{ij}b_{ij} + a_{ij}}{a_{ij}^2 + a_{ij}b_{ij} + a_{ij} + b_{ij}}\right),$$
$$i \neq j \tag{A.3}$$

with

$$a_{\text{cs}} = \frac{s + 2\delta}{d_{\text{c}}}, \quad b_{\text{cs}} = 1, \qquad a_{\text{sw}} = \frac{s}{d_{\text{c}} + 2\delta}, \quad b_{\text{sw}} = 1,$$

$$a_{\text{cs(w)}} = \frac{s + \delta}{d_{\text{c}}}, \quad b_{\text{cs(w)}} = \frac{d_{\text{c}} + 2\delta}{2d_{\text{c}}}.$$

The electrical properties of the material are taken into account by the composite Hamaker constant

$$A_{ij} = \left(A_{ii}^{1/2} - A_{jj}^{1/2} \right)^2, \tag{A.4}$$

which describes the interaction between the indicated components i and j (table 1). The corresponding Hamaker constants of identical entities in vacuum A_{ii} and in water $A_{ii}(\text{w})$, respectively, are listed in the second and third column of table 1 for some typical materials [22].

These attractive forces are opposed by electrostatic repulsion and steric interaction. Particles with functional groups like COONa and NH$_4$Cl dissociated in water have negative and positive surface potential Ψ, respectively. The energy of electrostatic repulsion of spherical, equally charged particles with surface potential Ψ and charge z of the counter ion reads [21]

$$E_{\text{el}}(s) = \frac{4k_{\text{B}}^2 T^2 \varepsilon_0 \varepsilon_r d_{\text{p}}}{e^2 z^2} \exp(-\kappa s) \left[\exp\left(\frac{ze\Psi}{2k_{\text{B}}T} \right) - 1 \right]^2 \left[\exp\left(\frac{ze\Psi}{2k_{\text{B}}T} \right) + 1 \right]^{-2} \tag{A.5}$$

where e is the charge of the electron, ε_0 and ε_r are the permittivity of vacuum and medium, respectively. The thickness of the screening layer is given by the inverse of the Debye–Hückel parameter

$$\kappa = \left(\frac{4\pi e^2}{\varepsilon_0 \varepsilon_r k_{\text{B}} T} \sum_n c_n z_n^2 \right)^{1/2} \tag{A.6}$$

which is determined by the concentration c and charge number z of the ions of sort n within the suspension.

A repulsive steric interaction arises whenever two particle shells begin to overlap. The potential energy of steric interaction can be calculated for small deformations by the Young's modulus E [21]

$$E_{\text{S}}(s) = \frac{E}{1.325} \left(2\delta - \frac{s}{2} \right)^{5/2} \left(\frac{d_{\text{p}}}{2} + \delta \right)^{1/2}. \tag{A.7}$$

Calculating this energy a Young's modulus of $E = 10^6$ Pa characteristic for polymer matrices [23] and biological membranes [24] was assumed.

References

[1] Weitschies W, Kötitz R, Bunte T and Trahms L 1997 Determination of relaxing or remanent nanoparticle magnetization provides a novel binding-specific technique for the evaluation of immunoassays *Pharm. Pharmacol. Lett.* **7** 1–4

[2] Kötitz R, Weitschies W, Trahms L, Brewer W and Semmler W 1999 Determination of the binding reaction between avidin and biotin by relaxation measurements of magnetic nanoparticles *J. Magn. Magn. Mater.* **194** 62–8

[3] Chemla Y R, Grossman H L, Poon Y, McDermott R, Stevens R, Alper M D and Clarke J 2000 Ultrasensitive magnetic biosensor for homogeneous immunoassay *Proc. Natl Acad. Sci.* **97** 14268–72

[4] Enpuku K and Minotani T 2001 Biological immunoassay with high T_C superconducting quantum interference device (SQUID) magnetometer *IEICE Trans. Electron.* E **84-C** 43–8

[5] Vrba J, Nenonen J and Trahms L 2006 Biomagnetism *The SQUID Handbook* (*Applications of SQUIDs and SQUID systems* vol II) ed J Clarke and A Braginski (Weinheim: Wiley) pp 269–389

[6] Matz H, Drung D, Hartwig S, Groß H, Kötitz R, Müller W, Vass A, Weitschies W and Trahms L 1998 A SQUID measurement system for immunoassays *Appl. Supercond.* **6** 577–83

[7] Kötitz R, Fannin P C and Trahms L 1995 Time domain study of Brownian and Néel relaxation in ferrofluids *J. Magn. Magn. Mater.* **149** 42–6

[8] Kötitz R, Trahms L, Koch H and Weitschies W 1995 Ferrofluid relaxation for biomagnetic imaging: Baumgartner C, Deecke L, Williamson S J (Hrsg.) *Biomagnetism: Fundamental Research and Clinical Applications* (Amsterdam: Elsevier Science)

[9] Lange J, Kötitz R, Haller A, Trahms L, Semmler W and Weitschies W 2002 Magnetorelaxometry—a new binding specific detection method based on magnetic nanoparticles *J. Magn. Magn. Mater.* **252** 381–3

[10] Grossman H L, Myers W R, Vreeland V L, Bruehl R, Alper M D, Bertozzi C R and Clarke J 2004 Detection of bacteria in suspension by using a superconducting quantum interference device *Proc. Natl Acad. Sci.* **101** 134

[11] Eberbeck D, Hartwig S, Steinhoff U and Trahms L 2003 Description of the magnetization decay in ferrofluids with a narrow particle size distribution *Magnetohydrodynamics* **39** 77–83

[12] Street R and Wooley J C 1949 A study of magnetic viscosity *Proc. Phys. Soc.* A **62** 562–72

[13] Street R and Brown S D 1994 Magnetic viscosity, fluctuation fields, and activation energies *J. Appl. Phys.* **76** 6386–90

[14] Brown W F 1963 Thermal fluctuations of a single-domain particle *J. Appl. Phys.* **34** 1319–20

[15] Néel M L 1949 Théorie du trainage magnétique des ferromagnétiques en grains fin avec applications aux terres cuites *Ann. Géophys.* **5** 99–136

[16] Shliomis M I and Raikher Y L 1980 Experimental investigations of magnetic fluids *IEEE Trans. Magn.* **16** 237–50

[17] Chantrell R W, Hoon S R and Tanner B K 1983 Time-dependent magnetization in fine-particle ferromagnetic systems *J. Magn. Magn. Mater.* **38** 133–41

[18] Berkov D V and Kötitz R 1996 Irreversible relaxation behavior of a general class of magnetic systems *J. Phys.: Condens. Matter* **8** 1257–66

[19] Eberbeck D, Bergemann C, Hartwig S, Steinhoff U and Trahms L 2005 Binding kinetics of magnetic nanoparticles on latex beads and yeast cells studied by magnetorelaxometry *J. Magn. Magn. Mater.* **289** 435–8

[20] Eberbeck D, Bergemann C, Hartwig S, Steinhoff U and Trahms L 2004 Binding kinetics of magnetic nanoparticles on latex beads studied by magnetorelaxometry *Appl. Organomet. Chem.* **18** 542–7

[21] Sonntag H 1977 *Lehrbuch der Kolloidwissenschaft* (Berlin: VEB Deutscher Verlag der Wissenschaften)

[22] Lyklema J 1993 *Fundamentals of Interface and Colloid Science* vol 1, *Fundamentals* (London: Academic)

[23] Abu-Lail N I 2003 The effect of biopolymer properties on bacterial adhesion: an atomic force microscopy (AFM) study *PhD Thesis* Polytechnic Institute Worcester

[24] Oberdisse J 2002 Structure and rheological properties of latex–silica nanocomposite films: stress–strain isotherms *Macromolecules* **35** 9441–50

[25] Ramirez L P and Landfester K 2003 Magnetic polystyrene nanoparticles with a high magnetite content obtained by miniemulsion processes *Macromol. Chem. Phys.* **204** 22–31

[26] Freshney R I 2000 *Culture of Animal Cells* 4th edn (New York: Wiley) p 103

[27] Cohen I R 1967 Natural and immune human antibodies reactive with antigens af virulent Neisseria gonorrhoeae: immunoglobulins G, M, and A *J. Bacteriol.* **94** 141–8

[28] Gaafar H A and D'Arcangelis D C 1976 Fluorescent antibody test for the serological diagnosis of Gonorrhea *J. Clin. Microbiol.* **3** 438–42

[29] Koneracka M, Kopčanský P, Timko M, Ramchand C N, de Sequeira A and Trevan M 2002 Direct binding procedure of proteins and enzymes to fine magnetic particles *J. Mol. Catal.* B **18** 13–8

[30] Eberbeck D, Bergemann Ch, Wiekhorst F and Glöckl G 2005 Quantification of aggregates of magnetic nanoparticles in different suspension media by magnetorelaxometry *Magnetohydrodynamics* **41** 305–16

[31] Wang Z and Holm C 2003 Structure and magnetic properties of polydisperse ferrofluids: a molecular dynamics study *Phys. Rev.* E **68** 041401

[32] Koolman J and Röhm K H 1998 *Taschenatlas der Biochemie* (Stuttgart: Thieme) p 281

[33] Wagner J, Autenrieth T and Hempelmann R 2002 Core–shell particles consisting of cobalt ferrite and silica as model ferrofluids [$CoFe_2O_4$–SiO_2 core–shell particles] *J. Magn. Magn. Mater.* **252** 4–6